SANDIA REPORT
SAND2004–3926
Unlimited Release
August 2004

Rock Penetration: Finite Element Sensitivity and Probabilistic Modeling Analyses

A. F. Fossum

Prepared by
Sandia National Laboratories
Albuquerque, New Mexico 87185 and Livermore, California 94550

Sandia is a multiprogram laboratory operated by Sandia Corporation, a Lockheed Martin Company, for the United States Department of Energy under Contract DE-AC04-94AL85000.

Issued by Sandia National Laboratories, operated for the United States Department of Energy by Sandia Corporation.

Available to DOE and DOE contractors from
Office of Scientific and Technical Information
P.O. Box 62
Oak Ridge, TN 37831

Prices available from (615) 576-8401, FTS 626-8401

Available to the public from
National Technical Information Service
U.S. Department of Commerce
5285 Port Royal Rd
Springfield, VA 22161

NTIS price codes
Printed copy: A03
Microfiche copy: A01

SAND2004-3926
Unlimited Release
Printed August 2004

Rock Penetration: Finite Element Sensitivity and Probabilistic Modeling Analyses

A. F. Fossum
Geoscience and Environment Center

Sandia National Laboratories
P.O. Box 5800
Albuquerque, NM 87185-0750

Abstract

This report summarizes numerical analyses conducted to assess the relative importance on penetration depth calculations of rock constitutive model physics features representing the presence of microscale flaws such as porosity and networks of microcracks and rock mass structural features. Three-dimensional, nonlinear, transient dynamic finite element penetration simulations are made with a realistic geomaterial constitutive model to determine which features have the most influence on penetration depth calculations. A baseline penetration calculation is made with a representative set of material parameters evaluated from measurements made from laboratory experiments conducted on a familiar sedimentary rock. Then, a sequence of perturbations of various material parameters allows an assessment to be made of the main penetration effects. A cumulative probability distribution function is calculated with the use of an advanced reliability method that makes use of this sensitivity database, probability density functions, and coefficients of variation of the key controlling parameters for penetration depth predictions. Thus the variability of the calculated penetration depth is known as a function of the variability of the input parameters. This simulation modeling capability should impact significantly the tools that are needed to design enhanced penetrator systems, support weapons effects studies, and directly address proposed HDBT defeat scenarios.

This page intentionally left blank.

Table of Contents

Abstract 3
Table of Contents 5
List of Tables 9
1. Executive Summary 11
1.2 Scientific Impact 12
1.3 Recommendations 12
2. Introduction 13
2.1 Technical Problem 13
2.2 Technical Issues 13
3. Rock Constitutive Model 14
3.1 Rock Model Overview 14
3.2 Rock Model Theory and User's Manual 17
4. Penetration Analyses 17
4.1 Rock Model Fitted to Salem Limestone Data 18
4.2 Penetration Analysis Results 22
4.5.3 Strain-Rate Sensitivity Turned Off 25
4.5.4 Compaction Turned Off 25
4.5.5 Kinematic Hardening Turned Off 25
4.5.6 Nonlinear Elasticity Turned Off 26
4.5.7 Lode Angle Dependence Turned Off 26
4.5.8 Joints Turned Off 27
4.5.9 Pressure Sensitivity Turned Off 27
4.5.10 Tensile Cracking Turned Off 28
4.5.11 Penetrator/Rock Coefficient of Friction Turned Off 30
4.3 Penetration Depth Versus Striking Velocity 30
4.4 Summary 30
4.5 Probabilistic Analyses 32
4.4.3 Deterministic Sensitivities 32
4.4.4 Probabilistic Results 33
5. Summary and Conclusions 35
6. Acknowledgments 35
7. References 36

This page left intentionally blank.

List of Figures

Figure 3-1 Rock model continuous yield surface - (a) three-dimensional view in principal stress space with the high pressure “cap” shown as a wire frame, (b) the meridional “side” view with the cap shown on the more compressive right-hand side of the plot, and (c) the octahedral view, which corresponds to looking down the hydrostat showing triaxial extension (TXE) and triaxial compression (TXC) stress states 16
Figure 3-2 Distinction between a yield surface and a limit surface (This sketch shows meridional profiles of an initial yield surface that might evolve from the initial surface. All achievable stress states, and thus all possible yield surfaces, are contained within the limit surface.) 16
Figure 3-3 Other yield surface shapes supported by the rock model by using a small subset of available parameters are shown in the top row. Row two shows available third invariant functions and their shapes in the octahedral plane for various ratios of triaxial extension strength to triaxial compression strength. 17
Figure 4-1 Rock model prediction versus measured data from hydrostatic compression tests conducted on Salem Limestone. 19
Figure 4-2 Rock model prediction versus measured triaxial compression and triaxial extension limit states from tests conducted on Salem Limestone. 20
Figure 4-3 Rock model prediction versus measured results for an unconfined compression test and a triaxial compression test conducted at 20 MPa confining pressure on Salem Limestone. 21
Figure 4-4 Rock model prediction versus measured results for a triaxial compression test on Salem Limestone, the load path followed during the test, and the evolving shape of the yield loci in the meridional plane. 21
Figure 4-5 Rock model prediction versus measured results of unconfined compressive strengths as a function of strain rate from Kolsky-bar strain-rate tests conducted on Salem Limestone. 22
Figure 4-6 Rock model prediction versus measured results for rock joint deformation in Salem Limestone. 22
Figure 4-7 Three-dimensional, penetrator-rock configuration used in the penetration analyses. 23
Figure 4-8 The plot on the left shows the velocity of the penetrator versus time while the plot on the right shows the penetration depth versus time for the initial baseline calculation. 24
Figure 4-9 This figure shows a contour plot of the equivalent (L2 Norm) strain rate in the rock surrounding the nose of the penetrator. 24
Figure 4-10 This figure shows a contour plot of the Lode Angle in the rock surrounding the penetrator. . 24
Figure 4-11 The plot on the left shows the velocity of the penetrator versus time while the plot on the right shows the penetration depth versus time. The baseline calculations are shown for comparison with the calculations with the strain-rate sensitivity turned off. 25
Figure 4-12 The plot on the left shows the velocity of the penetrator versus time while the plot on the right shows the penetration depth versus time. The baseline calculations are shown for comparison with the calculations with the compaction turned off. 26
Figure 4-13 The plot on the left shows the velocity of the penetrator versus time while the plot on the right shows the penetration depth versus time. The baseline calculations are shown for comparison with the calculations with the kinematic hardening turned off. 26
Figure 4-14 The plot on the left shows the velocity of the penetrator versus time while the plot on the right shows the penetration depth versus time. The baseline calculations are shown for comparison with the calculations with nonlinear elasticity turned off. 27
Figure 4-15 The top figure shows the velocity of the penetrator versus time while the bottom figure shows the penetration depth versus time. The baseline calculations are shown for comparison with the calculations with Lode Angle dependence turned off. 27

Figure 4-16 The plot on the left shows the velocity of the penetrator versus time while the plot on the right shows the penetration depth versus time. The baseline calculations are shown for comparison with the calculations with jointing turned off. 28
Figure 4-17 The figure on the left shows a contour plot of the cracked region emanating away from the penetrator when the joints are turned off. For comparison, the figure on the right shows the same contour plot when three orthogonal sets of joints are included (baseline case). 28
Figure 4-18 The plot on the left shows the velocity of the penetrator versus time while the plot on the right shows the penetration depth versus time. The baseline predictions are shown for comparison with the predictions made with the pressure dependence of shear strength turned off. 29
Figure 4-19 The plot on the left shows the velocity of the penetrator versus time while the plot on the right shows the penetration depth versus time. The baseline predictions are shown for comparison with the predections made with the tensile cracking turned off. 29
Figure 4-20 Tensile cracking results in more dilatational volume strain resulting in less penetration depth prediction because of increased frictional forces. This effect is relatively minor. 29
Figure 4-21 The plot on the left shows the velocity of the penetrator versus time while the plot on the right shows the penetration depth versus time. The baseline predictions are shown for comparison with the predections made with the friction between the rock and the penetrator turned off. There is nearly a 50% increase in predicted penetration depth. 30
Figure 4-22 Shown is penetration depth versus striking velocity. The projectile bounces off of the target for a striking velocity of 10 m/s. 31
Figure 4-23 This figure shows the relative impact that the physics features of the rock model have on penetration depth predictions. The magnitude represents the percentage change from the baseline calculation when the feature is turned off. 31
Figure 4-24 Deterministic relative response sensitivities 34
Figure 4-25 This is a plot of the Cumulative Distribution Function (CDF) for penetration depth. 34
Figure 4-26 Probabilistic importance factors 34

List of Tables

Table 4-1. Baseline rock model parameters for Salem Limestone 19
Table 4-2. Parameter Distributions and Statistics 32

This page left intentionally blank.

1. Executive Summary

The relative importance is determined of rock model parameters representing the presence of microscale flaws such as porosity and networks of microcracks and rock mass structural features on depth of penetration calculations for a weapon projectile. After the determination of key parameters, which represent the dominant deformation mechanisms controlling penetration resistance, a probabilistic analysis is undertaken with an advanced reliability method that incorporates the deterministic tools developed in this project to quantify the uncertainty of the predicted penetration depth response caused by the uncertainty in the input material parameters representing the controlling mechanisms. The key parameters containing uncertainty are then ranked according to their probabilistic importance factors. Thus, if it were desired to decrease the uncertainty in the predicted penetration response the analyst has the option of attempting to reduce the uncertainty of the most important parameters, perhaps by additional testing.

The constitutive model used in the analyses for rock behavior during penetration is developed to take into account the principal deformation mechanisms controlling penetration as well as up-scaling of these processes to account for rock-mass and structural features that could influence a penetration event. For computational tractability, and to allow relatively straightforward model parameterization using standard laboratory tests, the constitutive model is constructed to strike a balance between first-principals micro-mechanics and phenomenological modeling strategies. The over-arching goal of the constitutive modeling effort is to provide a unified general-purpose constitutive model that can be used for any geological or rock-like material and one that is predictive over a wide range of porosities and strain rates.

The following conclusions are drawn from more than 30 penetration finite element analyses:

1) The most important physics features represented in the rock model from the standpoint of predicting penetration in order of importance are *a*) pressure sensitivity of yield, *b*) the coefficient of friction between the penetrator and the rock, *c*) ubiquitous rock jointing, *d*) strain-rate sensitivity, and *e*) pore collapse. Playing lesser roles are tensile cracking, kinematic hardening, Lode Angle dependence of yield, and nonlinear elasticity.
2) When the important physics features are included in the model, the material parameters representing the physics that are most important *deterministically* in order of importance are *a*) strain-rate sensitivity, *b*) ubiquitous rock jointing, *c*) the coefficient of friction between the penetrator and the rock, *d*) porosity, and *e*) pressure sensitivity of yield.
3) From a *probabilistic* standpoint the order of importance changes because of the degree of uncertainty associated with the parameters. The key probabilistic importance factors in order of importance are *a*) ubiquitous rock jointing, *b*) strain-rate sensitivity, *c*) the coefficient of friction between the penetrator and the rock, *d*) pressure sensitivity of yield, and *e*) pore collapse. Because all rocks have inherent uncertainty it is the

probabilistic importance factors, which combine deterministic sensitivities with uncertainty, that are perhaps the most important from a practical standpoint.
4) Penetration depth increases with increasing striking velocity. If the striking velocity is too low, the penetrator will ricochet off the target.
5) The influence of pore collapse on penetration increases slightly with increasing striking velocity because of the difference in the loadpath followed with increasing striking velocity.

1.2 Scientific Impact

The scientific impact of the findings of this research effort on penetration prediction is that it is more important to include the major physics phenomena governing penetration in a rock model used to model penetration than it is to evaluate a full physics model that characterizes the complete stress-strain curves obtained in laboratory testing. Also, the uncertainties in the parameters associated with the main physics for Salem Limestone, which is a rock with relatively low uncertainty compared with many sedimentary rocks, translate to 27 % uncertainty in penetration depth predictions with 98% confidence. If a target rock can be identified through telemetry and/or other means it may be possible to use this information to identify a rock classification from which a known rock characterization for an analog rock can be used to make penetration depth predictions as a function of striking velocity with relatively high confidence from only a minimal amount of laboratory testing.

1.3 Recommendations

It is recommended that a suite of candidate target rock types be characterized with the minimum amount of testing to evaluate the key parameters representing the important physics governing penetration resistance for general categories of rock types likely to be identified through direct as well as indirect means.

2. Introduction

2.1 Technical Problem

To defeat a hard and deeply buried target (HDBT) a weapon must penetrate the target surface to sufficient depth so that energy coupling can be achieved between the rock and the penetrator. As a result of previous weapon design efforts a great deal of research has been directed recently toward penetration of cohesive soils, ice, and frozen soils. Nonetheless, there are regions where the soil cover is small relative to the size of the penetrator and thus it becomes necessary to penetrate the surface rock or attempt to soften the surface for a subsequent penetrator attack. Penetration of rock and rock rubble has not been researched sufficiently to elucidate the physics of rock penetration for these materials. The influence of such basic factors as porosity, hardness, geologic strata, fracture density, and surface weathering on penetration path and depth has been virtually unknown, resulting in a limited capability to model rock penetration in enough detail to support the design process.

2.2 Technical Issues

An earth penetrator induces mean stresses, and shear stresses that vary with space and time in the country rock surrounding the penetrator. Mean stresses and strain rates that occur during a penetration event affect the shear and crush strength of rock. The response of the rock near the penetrator is quite complex because the application of elevated mean stress and strain rates can dramatically alter the deformation mechanism of rocks.

Rocks accommodate inelastic deformations by two basic mechanisms: brittle fracture and pore compaction. Mean stress tends to suppress brittle fracturing, but enhances pore compaction (if there is sufficient porosity in the rock and the initial crush strength can be exceeded). Similarly, increasing strain rates tends to increase shear and crush strengths. As rock fails, it can also expand volumetrically and/or compact depending on the deformation mechanism(s) leading to failure. Different stress paths and failure modes lead to different resistance forces applied to the penetrator. Knowledge of the deformation mechanisms in rock and the regimes in which they are important during penetration is essential to the development of appropriate constitutive models for rock penetration.

In addition to using the knowledge base of intact rock deformation, the modeling of penetration requires one to use information on rock structure that has a scale several times the penetrator diameter. This structure involves the natural variability of intact rock, the presence of natural joints and bedding planes, and possibly lithophysae, vugs, or other similar features. The effect of these features on penetration has heretofore been unknown. Joints, especially, are pervasive and ubiquitous in hard rock. There are few data on shear strength and friction characteristics of joints at loading rates approaching those during penetration.

Finally, there are issues related to the interface between the penetrator and rock. Frictional effects between the penetrator and the rock are not well characterized and they will be shown here to be a significant component of target resistance. The character of interface friction will also likely change significantly as a function of rock type, primarily as a result of differing mineral hardness and shear strength.

3. Rock Constitutive Model

For natural geomaterials, common features are the presence of microscale flaws such as porosity (which permits inelasticity even in purely hydrostatic loading) and networks of microcracks (leading to low strength in the absence of confining pressure and to noticeable nonlinear elasticity, rate-sensitivity, and differences in material deformation under triaxial extension compared with triaxial compression).

To be computationally tractable and to allow relatively straightforward model parameterization using standard laboratory tests, the rock constitutive model developed *(Fossum and Brannon, 2004a*) strikes a balance between first-principals micro-mechanics and phenomenological, homogenized, and semi-empirical modeling strategies. The over-arching goal is to provide a unified general-purpose constitutive model that can be used for any geological or rock-like material that is predictive over a wide range of porosities and strain rates. Being a unified theory, the rock model can simultaneously model multiple failure mechanisms, or (by using only a small subset of the available parameters) it can duplicate simpler idealized yield models such as classic Von Mises plasticity and Mohr-Coulomb failure.

3.1 Rock Model Overview

Dilatation and compaction strains are allowed to occur simultaneously to be consistent with observed experimental observations on the micro scale. For stress paths that result in brittle deformation, failure is associated ultimately with the attainment of a peak stress and subsequently work-softening deformation. Tensile or extensile microcrack growth dominates the micromechanical processes that result in macroscopically volume increasing strains even when all principal stresses are compressive. At higher pressures, these processes can undergo strain-hardening deformation associated with macroscopically compactive volumetric strain (i.e., pore collapse).

The rock model (*Fossum and Brannon, 2004a, 2004b)* predicts observed material response without explicitly addressing how the material behaves as it does, and thus it reflects subscale inelastic phenomena *en ensemble* by phenomenologically matching observed data to interpolation functions. Considerations guiding the structure of the rock model's material response functions are (1) consistency with microscale theory, (2) computational tractability, (3) suitability to capture trends in characterization data, and (4) physics-based judgments about how a material should behave in application domains where controlled experimental data cannot be obtained.

Growth and coalescence of microcracks and pores provide the primary source of inelastic deformation in geological materials (or in rock-like materials such as concrete and ceramics). Under massive confining pressures, inelasticity could include plasticity in its traditional dislocation sense or, more generally, might result from other microphysical mechanics, (internal locking, phases transformation, twinning, etc.).

The rock model makes no explicit reference to microscale properties such as porosity, grain size, or crack density. Instead, the overall combined effects of the microstructure result from casting the macroscale theory in terms of macroscale variables that are realistic to measure in the laboratory. The rock model falls into the category of a hybrid model that has features of a microphysical model and a purely phenomenological model. In this sense a hybrid model mimics the microscale processes with evolution equations evaluated from macroscopic measurements. The rock model presumes that there exists a convex contiguous elastic domain of stress states small enough so that the material response can be considered elastic. The boundary of the elastic domain characterizes the yield surface. Aside from supporting kinematic hardening, the rock model is isotropic, which means that the criterion for the onset of plasticity depends only on the three principal values of the stress tensor, $(\sigma_1, \sigma_2, \sigma_3)$, but not on the principal directions.

Consequently, as illustrated in Figure 3-1, the yield surface may be visualized as a 2D surface embedded in a 3D space where the axes are the principal stresses. The interior of this surface represents the elastic domain.

While the yield surface represents the boundary of elastically obtainable stress states, a limit surface represents the boundary of stresses quasi-statically obtainable by any means, elastic or plastic. Points outside a *yield* surface might be attainable through a hardening process, but points outside the *limit* surface are not attainable by any quasi-static process. Points on the *limit* surface mark the onset of material softening. Consequently, a state on the *limit* surface is attainable at least once, but might not be attainable thereafter. The rock model simulates material response only up to the limit state. It does not simulate subsequent softening, if any, because softening usually induces a change in type of the partial differential equations for momentum balance, which therefore requires a response from the host code driving the rock model to alter its solution algorithm (perhaps by inserting void or by activating special elements that accommodate displacement discontinuities). Since the rock model does not directly model material softening, the limit surface may be regarded as fixed. Because the limit surface contains all attainable stress states, it follows that the set of all possible yield surfaces falls within the limit surface as shown in Figure 3-2. Even though developed primarily for geological applications, the rock model is truly a unification of many classical plasticity models. For example, by using only a small subset of available parameters, one can instruct the rock model to behave like many classical models some of which appear in Figure 3-3.

Under high strain rates, elastic material response occurs almost instantaneously, but the physical mechanisms that give rise to observable inelasticity cannot proceed instantaneously. Materials have inherent “viscosity” that retards the rate at which damage accumulates. For example, cracks grow at a finite speed. If a stress level induces crack growth, the quasi-static solution for material damage will not be realized unless sufficient time elapses to permit the cracks to change length. Likewise, pore collapse takes finite time. When the cracks are growing towards the quasi-static solution, the stress will also

decrease toward the quasi-static solution. Until sufficient time has elapsed the stress state will lie outside the yield surface. If the applied strain were released during this damage accumulation period, the total damage would be ultimately lower than it would have been under quasi-static loading through the same strain path.

A generalized strain-rate-sensitive formulation is developed in which the user specifies a "relaxation" parameter governing the characteristic speed at which the material can respond inelastically.

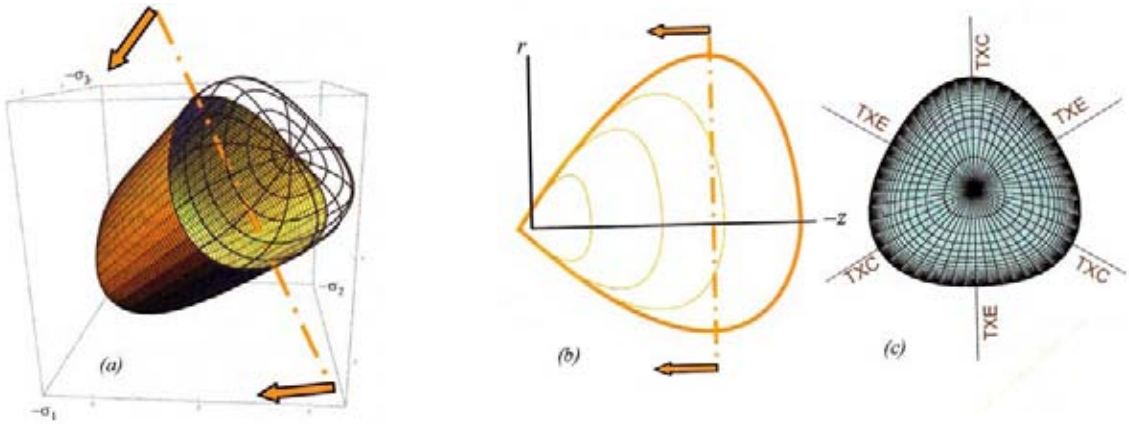

Figure 3-1 Rock model continuous yield surface - (a) three-dimensional view in principal stress space with the high pressure "cap" shown as a wire frame, (b) the meridional "side" view with the cap shown on the more compressive right-hand side of the plot, and (c) the octahedral view, which corresponds to looking down the hydrostat showing triaxial extension (TXE) and triaxial compression (TXC) stress states (from *Fossum and Brannon, 2004a*)

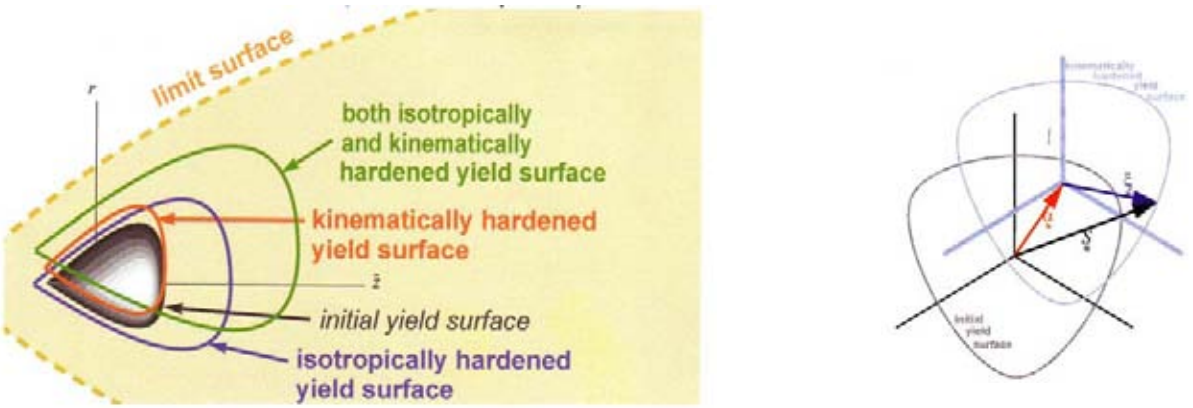

Figure 3-2 Distinction between a yield surface and a limit surface (This sketch shows meridional profiles of an initial yield surface that might evolve from the initial surface. All achievable stress states, and thus all possible yield surfaces, are contained within the limit surface.) (from *Fossum and Brannon, 2004a*)

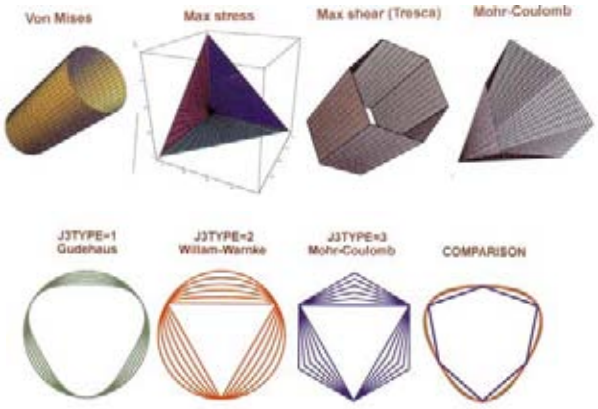

Figure 3-3 Other yield surface shapes supported by the rock model by using a small subset of available parameters are shown in the top row. Row two shows available third invariant functions and their shapes in the octahedral plane for various ratios of triaxial extension strength to triaxial compression strength**.** (from *Fossum and Brannon, 2004a*)

The characteristic time determined empirically provides flexibility in matching high strain-rate data for a wide range of rock types.

The rock model includes the option of including any number of ubiquitous rock joint sets. The rock joint development includes a nonlinear joint normal stiffness, a constant joint shear stiffness, spacing of joints in each set, orientation of the joint sets in terms of strike and dip, and joint aperture.

3.2 Rock Model Theory and User's Manual

The complete theoretical formulation of the rock model and user's guide can be found in *Fossum and Brannon (2004a)*, including discussions of the mathematical structure of the model, parameterization procedures, material parameter sets for various rocks, numerical solution scheme, verification, validation, and software quality assurance. A summary of the model can also be found in *Fossum and Brannon (2004b).*

4. Penetration Analyses

Nonlinear, three-dimensional, transient dynamic finite element analyses provide information for an ogive nose steel penetrator striking a rock with moderate porosity (8-9%). For this study, the rock model is fitted to quasi-static and dynamic laboratory data for Salem Limestone. The goals of these analyses were the following:

1) Determine the order of importance for penetration calculations of various model physics features and material parameters that are needed to describe the laboratory data.
2) Determine the uncertainty of the penetration depth predictions given the uncertainties in the important input parameters.

Recall from Section 3.1 that the rock model simulates material response only up to the limit state. The development of a softening capability is a work in progress in other programs, and thus, as of this writing, the ability to transition from a continuum to a discontinuum is not yet available. This modeling capability may be important because the material ahead of the penetrator breaks apart and a cratering region forms behind the penetrator because of rock fragmentation. To circumvent this difficulty for the present, a pilot hole is introduced into the rock ahead of the penetrator. Despite the presence of the pilot hole one can still assess the importance during the deceleration phase of the penetrator of the physical deformation mechanisms modeled and of various other model features on penetration depth predictions. It should be pointed out that other penetration solution strategies also avoid the fragmentation issue, such as the spherical cavity expansion procedure. Nonetheless, *Warren, Fossum, and Frew (2004)* demonstrate that the spherical cavity expansion procedure, using the rock model described above, can give very good predictions of penetration depth for a wide range of striking velocities for some materials.

In the remainder of this section, the rock model representation of the laboratory data for Salem Limestone will be shown followed by the penetration analysis results.

4.1 Rock Model Fitted to Salem Limestone Data

Nearly all of the rock model features are required to fit the matrix (intact) quasi-static and dynamic laboratory data for Salem Limestone as well as the rock joints. Thus, Salem Limestone turns out to be an ideal rock to use in these analyses to determine which of the features and many parameters are important in a penetration calculation. Moreover, this rock has been widely characterized and data are available to provide probability density functions for many of the elastic and strength parameters (e.g. *Fossum et al., 1995*).

Table 4-1 gives the baseline parameter set determined from quasi-static and dynamic laboratory data. The meaning of each of these parameters and how to determine them is described in detail in *Fossum and Brannon (2004a)*.

Figure 4-1 shows the rock model simulation of quasi-static hydrostatic compression experiments. Note the nonlinear elastic deformation exhibited during the unload-reload cycles. The bulk modulus increases with increasing pressure and decreases with increasing volumetric compaction strain. Figure 4-2 shows the rock model prediction of experimental triaxial compression and triaxial extension limit states. It is found that the triaxial extensile strength is approximately 70% of the triaxial compressive strength.

Table 4-1. Baseline rock model parameters for Salem Limestone

B0	B1	B2	B3	B4	G0	G1	G2	G3	G4
(Pa)	(Pa)	(Pa)	(Pa)	(ndim)	(Pa)	(ndim)	(1/Pa)	(Pa)	(ndim)
1.30E+10	4.25E+10	4.11E+08	1.20E+10	0.021	9.86E+09	0	0	0	0
RJS	RKS	RKN	A1	A2	A3	A4	P0	P1	P2
(m)	(Pa/m)	(Pa/m)	(Pa)	(1/Pa)	(Pa)	(rad)	(Pa)	(1/Pa)	(1/Pa^2)
0.00E+00	2.00E+13	1.00E+12	8.43E+08	2.73E-10	8.22E+08	1.00E-10	-3.14E+08	1.22E-10	1.28E-18
P3	CR	RK	RN	HC	CTI1	CTPS	T1	T2	T3
(1)	(ndim)	(ndim)	(Pa)	(Pa)	(Pa)	(Pa)	(s)	(1/s)	(ndim)
8.40E-02	6	0.72	1.20E+07	1.00E+11	3.00E+06	1.00E+06	4.00E-04	0.835	0
T4	T5	T6	T7	J3TYPE	A2PF	A4PF	CRPF	RKPF	SUBX
(1/s)	(Pa)	(s)	(Pa)	(ndim)	(1/Pa)	(rad)	(ndim)	(ndim)	
0.00E+00	0.00E+00	3.00E+00	0.00E+00	3	2.73E-10	1.00E-10	6	0.72	2
CN1	CN2	CN3	VM1	VM2	VM3	SP1	SP2	SP3	ST1
(Pa/m)	(Pa/m)	(Pa/m)	(m)	(m)	(m)	(m)	(m)	(m)	(Pa/m)
5.00E+09	5.00E+09	5.00E+09	4.80E-05	4.80E-05	4.80E-05	5.00E-02	5.00E-02	5.00E-02	5.00E+10
ST2	ST3								
(Pa/m)	(Pa/m)								
5.00E+10	5.00E+10								

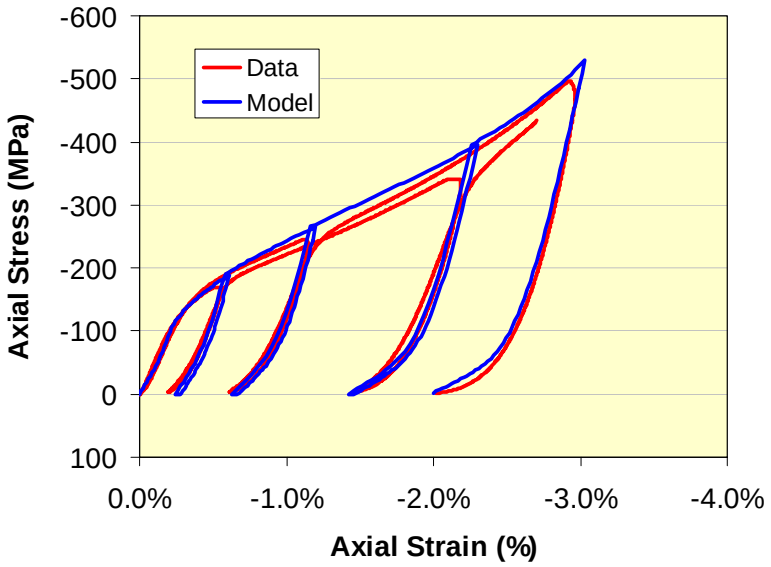

Figure 4-1 Rock model prediction versus measured data from hydrostatic compression tests conducted on Salem Limestone.

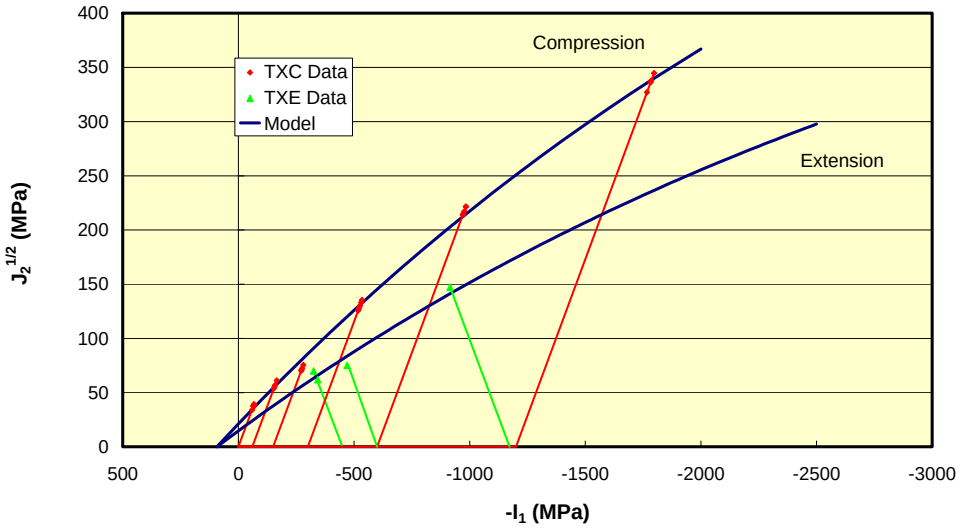

Figure 4-2 Rock model prediction versus measured triaxial compression and triaxial extension limit states from tests conducted on Salem Limestone.

Figure 4-3 shows the rock model prediction of an unconfined compression test and a triaxial compression test conducted at 20 MPa confining pressure. The model accurately captures the initial compaction caused by pore collapse and then transitions to dilatation-dominated deformation. Figure 4-4 shows the rock model prediction versus measured results for a triaxial compression test conducted at 400 MPa confining pressure. The load path is shown as well as a number of yield envelopes that correspond to various points of the axial stress versus volume strain curve recorded during the test. Again the model represents clearly the micromechanical processes that occur during the loading process, including pore collapse resulting in inelastic volumetric compaction, microcrack and microvoid growth resulting in inelastic volumetric dilatation. The model allows these deformation mechanisms to occur simultaneously. When the pore space becomes depleted the dilatational mechanisms begin to dominate. Figure 4-4 shows where these phenomena occur on the evolving yield surface. Figure 4-5 shows the rock model prediction versus measured results for a series of Kolsky-bar strain-rate tests conducted on unconfined compression specimens (*Frew et al., 2001)*. Unconfined compressive strength increases with increasing strain rate and, as seen in Figure 4-5, it doubles as the rate increases from $1x10^{-5}$ s^{-1} to 100 s^{-1}. Figure 4-6 shows the rock model prediction of an experimental unconfined compression test of a specimen containing a rock joint. The first curve in this figure is of the matrix rock while the third curve is of the matrix rock and the rock joint. The second curve is found from subtracting the first curve from the third curve to get the rock joint deformation.

These model comparisons with measured results illustrate that the model behaves as intended. Computationally tractable and accurate predictions can be made on broad temporal and spatial scales because the rock model captures salient microphysical phenomena en ensemble through phenomenological governing equations that can be parameterized from standard laboratory scale experiments.

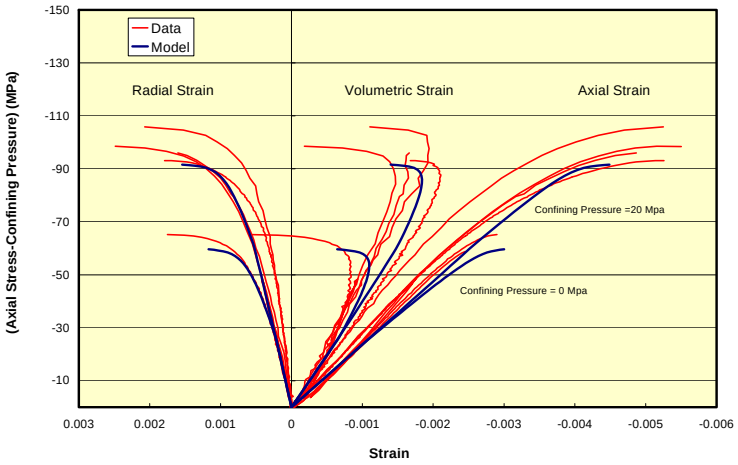

Figure 4-3 Rock model prediction versus measured results for an unconfined compression test and a triaxial compression test conducted at 20 MPa confining pressure on Salem Limestone.

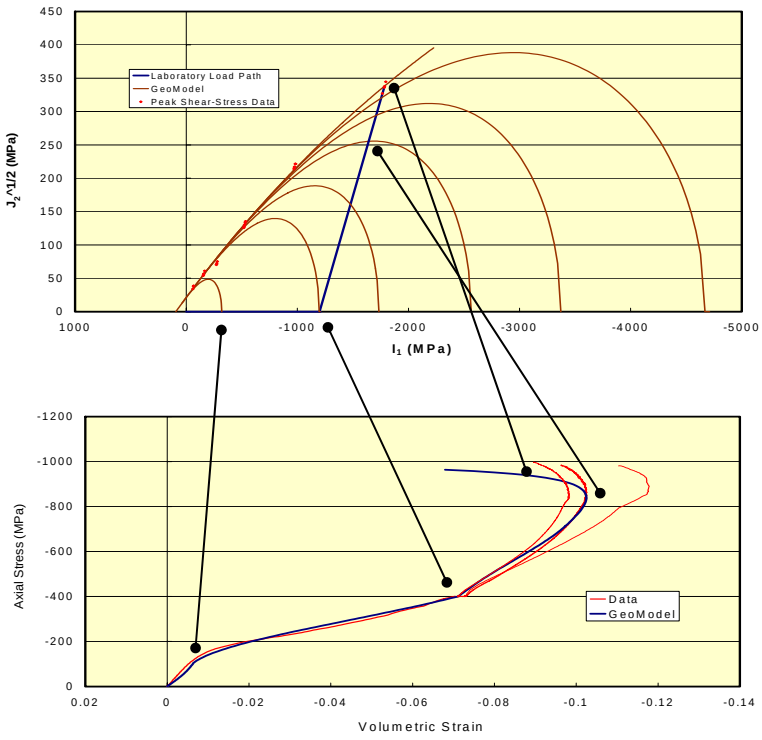

Figure 4-4 Rock model prediction versus measured results for a triaxial compression test on Salem Limestone, the load path followed during the test, and the evolving shape of the yield loci in the meridional plane.

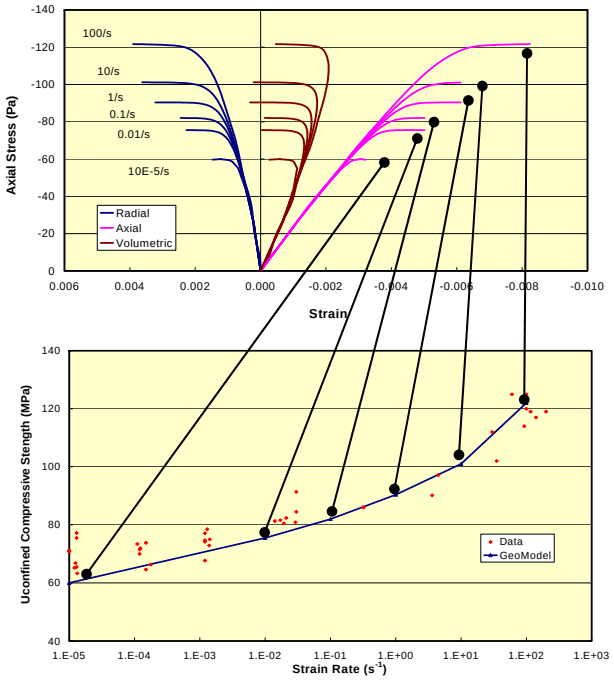

Figure 4-5 Rock model prediction versus measured results of unconfined compressive strengths as a function of strain rate from Kolsky-bar strain-rate tests conducted on Salem Limestone.

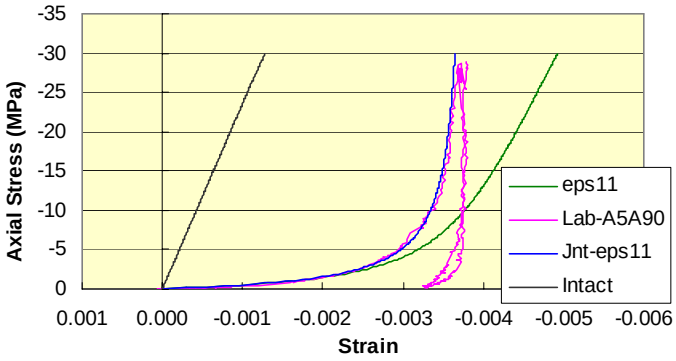

Figure 4-6 Rock model prediction versus measured results for rock joint deformation in Salem Limestone.

4.2 Penetration Analysis Results

The three-dimensional penetrator-rock configuration used in these analyses is shown in Figure 4-7. The mesh, which takes advantage of symmetry planes, contains 11,511 hexahedral elements and 13,947 nodes. The penetrator is assumed to be elastic for these analyses.

The first analysis is for the fully characterized model with parameters as listed in Table 4.1 and for a penetrator striking velocity of 250 m/s. The velocity of the penetrator versus time and the penetration depth versus time are plotted in Figure 4-8.

Figure 4-9 shows a plot of the equivalent strain rate at points in the rock near the penetrator. A significant volume of material has undergone strain rates exceeding 500 per second. This suggests that there may be a significant strain-rate effect on penetration since the unconfined compressive strength is known to double when the strain rate reaches about 100 per second.

Figure 4-10 shows a contour plot of the Lode angle present in the rock as the penetrator advances into the rock. The Lode angle is an indicator of the type of stress state that exists in a body while it is loaded. A value of –30 degrees represents a triaxial extension stress state while a value of 30 degrees represents a triaxial compression stress state. A value of zero represents pure shear. As seen in Figure 4-10, the stress state in the rock is quite complex but is predominantly in a state of triaxial compression (red in Figure 4-10), though there are significant regions diagonally ahead of the penetrator that are stressed in a state of pure shear (green in Figure 4-10).

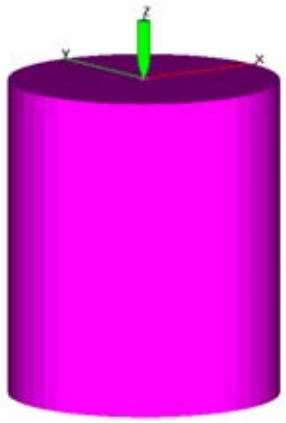

Figure 4-7 Three-dimensional, penetrator-rock configuration used in the penetration analyses.

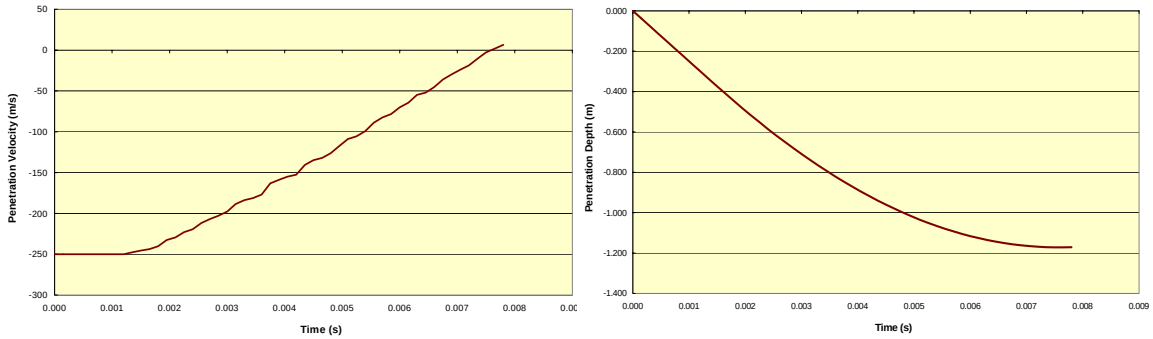

Figure 4-8 The plot on the left shows the velocity of the penetrator versus time while the plot on the right shows the penetration depth versus time for the initial baseline calculation.

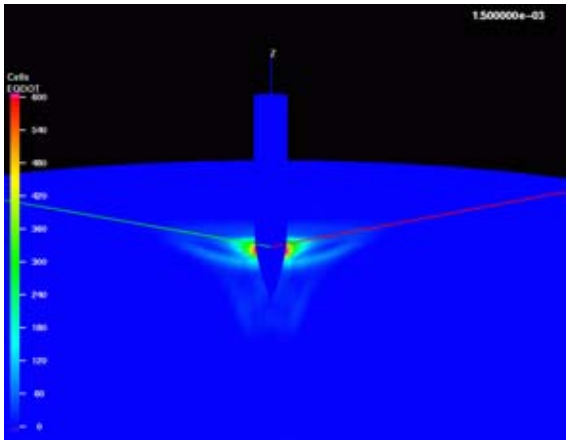

Figure 4-9 This figure shows a contour plot of the equivalent (L2 Norm) strain rate in the rock surrounding the nose of the penetrator.

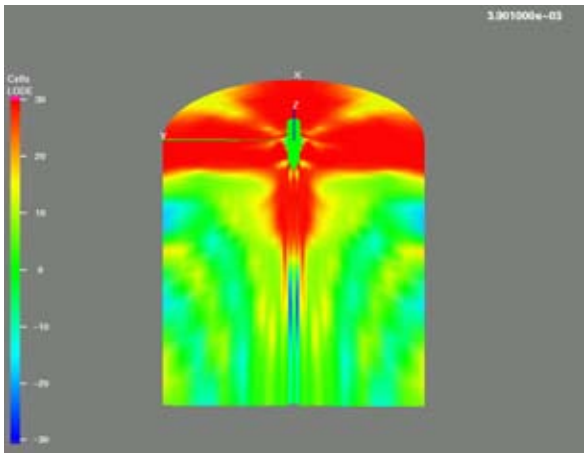

Figure 4-10 This figure shows a contour plot of the Lode Angle in the rock surrounding the penetrator.

4.5.3 Strain-Rate Sensitivity Turned Off

To determine the importance of strain-rate sensitivity on penetration resistance, a prediction is made with the parameters controlling rate sensitivity set to zero (parameters T1, T2, and T6 are set to zero in Table 4-1). The strain-rate insensitive and baseline predictions are shown in Figure 4-11 for penetration velocity and penetration depth. As shown in the figure, the penetration depth increases by 6% when strain-rate sensitivity of strength is not included in the calculation. This is because the strength increases with increasing strain rate.

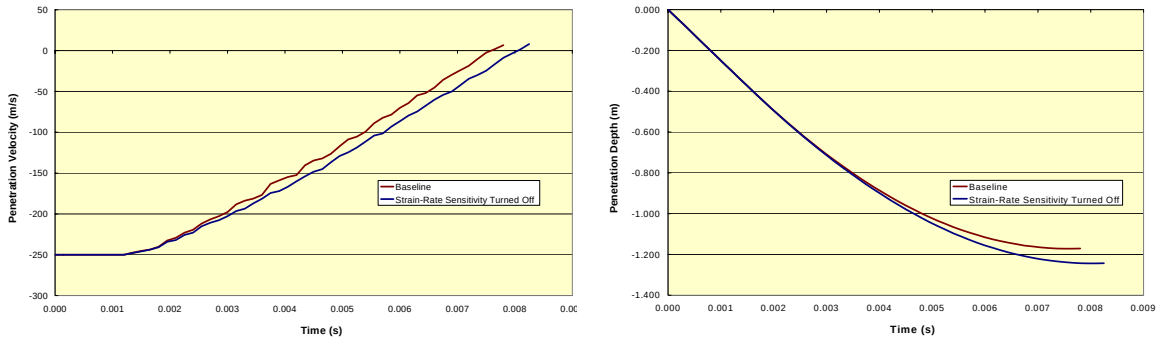

Figure 4-11 The plot on the left shows the velocity of the penetrator versus time while the plot on the right shows the penetration depth versus time. The baseline calculations are shown for comparison with the calculations with the strain-rate sensitivity turned off.

4.5.4 Compaction Turned Off

The effect of pore collapse on penetration resistance is determined by setting the parameter controlling compaction to a high number (the magnitude of parameter P0 in Table 4-1, is increased an by an order of magnitude). The resulting velocity and penetration depth predictions are shown with the baseline predictions in Figure 4-12. As shown in the figure, when pore collapse is turned off there is a decrease in penetration depth of 4%. This is because the volume of space that is created by compaction in the baseline prediction is not available for the penetrator when compaction is turned off.

4.5.5 Kinematic Hardening Turned Off

Figure 4-13 shows that kinematic hardening affects the prediction of penetration depth by less that 1%, and thus it is not very important in these calculations. Parameter RN in Table 4-1 is set to zero in these calculations.

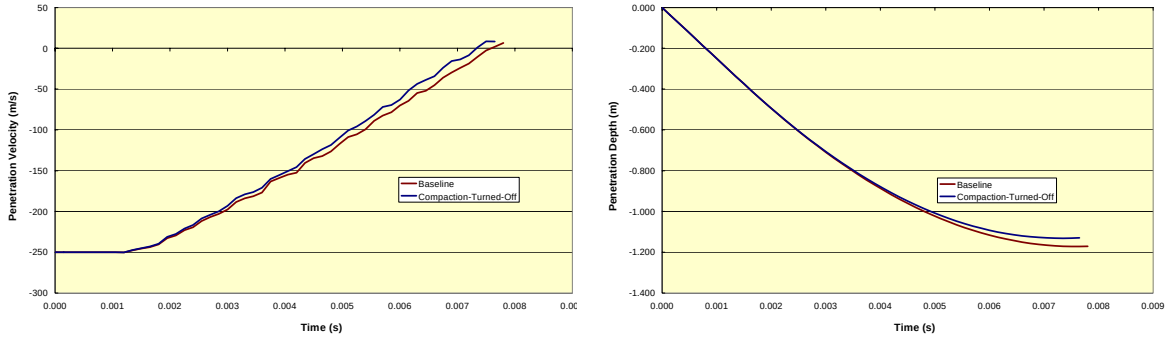

Figure 4-12 The plot on the left shows the velocity of the penetrator versus time while the plot on the right shows the penetration depth versus time. The baseline calculations are shown for comparison with the calculations with the compaction turned off.

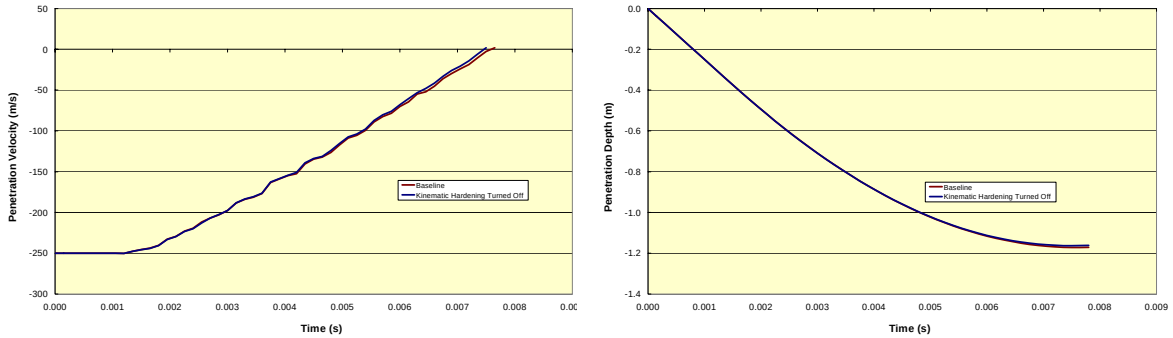

Figure 4-13 The plot on the left shows the velocity of the penetrator versus time while the plot on the right shows the penetration depth versus time. The baseline calculations are shown for comparison with the calculations with the kinematic hardening turned off.

4.5.6 Nonlinear Elasticity Turned Off

Figure 4-14 illustrates that nonlinear elasticity, which is caused primarily by recoverable opening and closing of microcracks, does not play an important role in penetration depth predictions, contributing less than 0.1% to the calculation.

4.5.7 Lode Angle Dependence Turned Off

Lode-angle dependence of yield strength is not very important in penetration calculations as evidenced in Figure 4-15. There is less that 1% difference between the baseline prediction and the prediction made without Lode-angle dependence. The reason for this can be seen in the Lode angle contour plot of Figure 4-10, in which most of the yielded material surrounding the advancing penetrator is stressed in a state of triaxial compression. This calculation is made with RK equal to 1, and JTYPE equal to 2 in Table 4-1. RK is the ratio of triaxial extension strength to triaxial compression strength. JTYPE equal to 2 specifies that a Willam-Warnke third invariant function is used. With RK equal to 1, the Willam-Warnke third invariant function takes the shape of a circle in the octahedral plane (illustrated in Figure 3-3). The baseline calculations are made with a JTYPE equal to 3 specifying a Mohr-Coulomb third invariant function. With RK equal to

1 the Mohr-Coulomb third invariant function takes the shape of a hexagon and is thus dependent on the Lode angle.

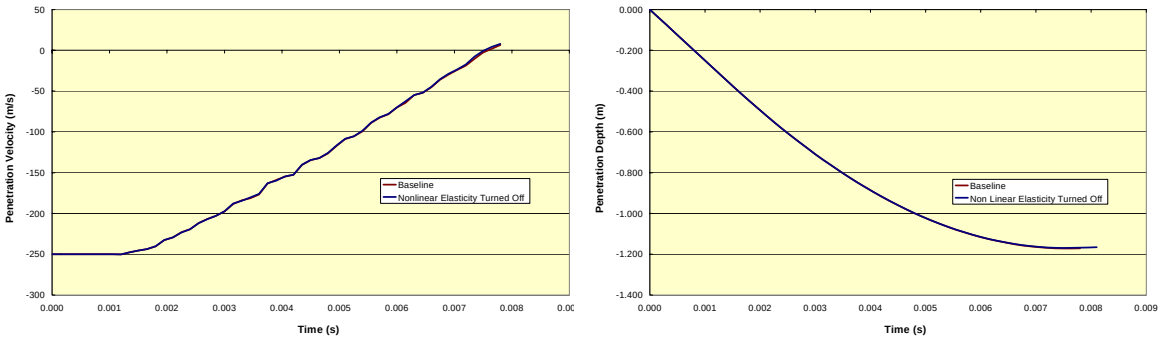

Figure 4-14 The plot on the left shows the velocity of the penetrator versus time while the plot on the right shows the penetration depth versus time. The baseline calculations are shown for comparison with the calculations with nonlinear elasticity turned off.

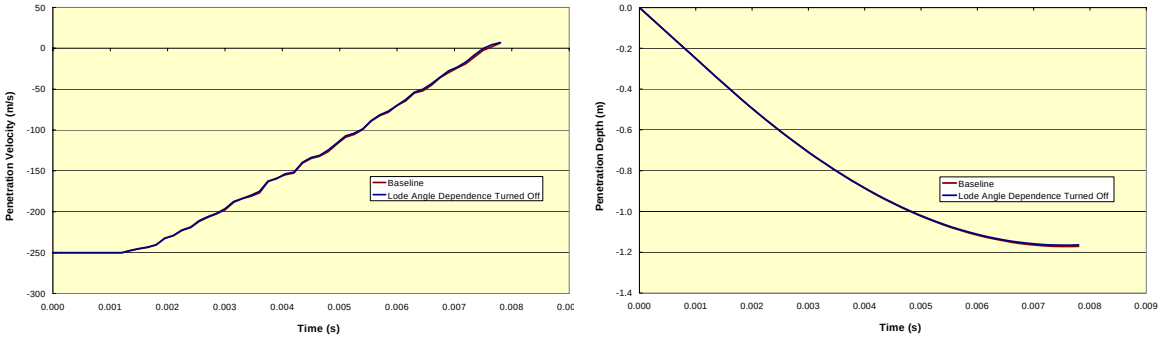

Figure 4-15 The top figure shows the velocity of the penetrator versus time while the bottom figure shows the penetration depth versus time. The baseline calculations are shown for comparison with the calculations with Lode Angle dependence turned off.

4.5.8 Joints Turned Off

Figure 4-16 illustrates the importance of rock jointing. Not including the rock joints resulted in 28% less penetration. One of the effects of including three orthogonal joint sets can clearly be seen in Figure 4-17 on the cracking region. Note the lack of angular symmetry of the cracking region when jointing is included in the calculation. However, the most important contribution of the rock joints is the reduced compliance of the rock mass, which facilitates projectile penetration. In the analysis, the joints were turned off by setting all of the parameters to zero in the last two rows of Table 4-1.

4.5.9 Pressure Sensitivity Turned Off

The most important physical feature of a rock with respect to penetration resistance is its ability to get stronger with increasing mean stress. Figure 4-18 shows that if pressure dependence is turned off and only the unconfined compressive strength is used, the predicted penetration depth increases by 68%. In addition to being weaker in shear

strength when pressure dependence is turned off, the material also does not expand during yielding and thus without bulking there is more room for penetration to occur. The pressure dependence is turned off by setting the parameter A2 equal to zero in Table 4-1.

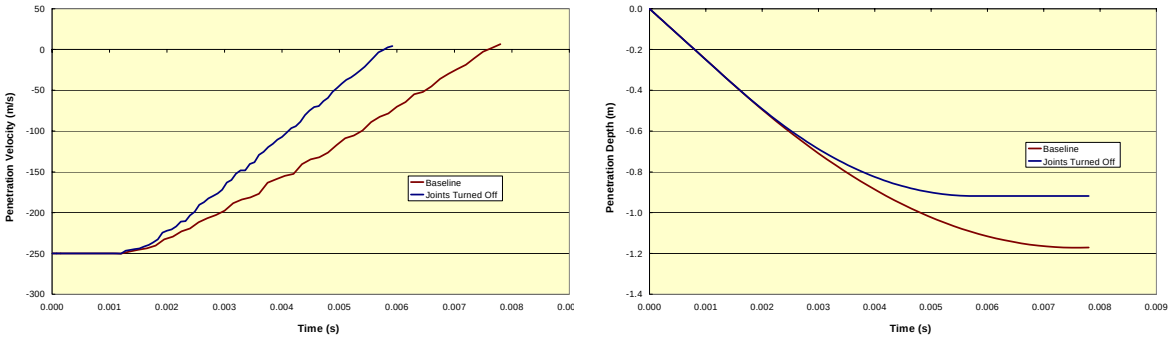

Figure 4-16 The plot on the left shows the velocity of the penetrator versus time while the plot on the right shows the penetration depth versus time. The baseline calculations are shown for comparison with the calculations with jointing turned off.

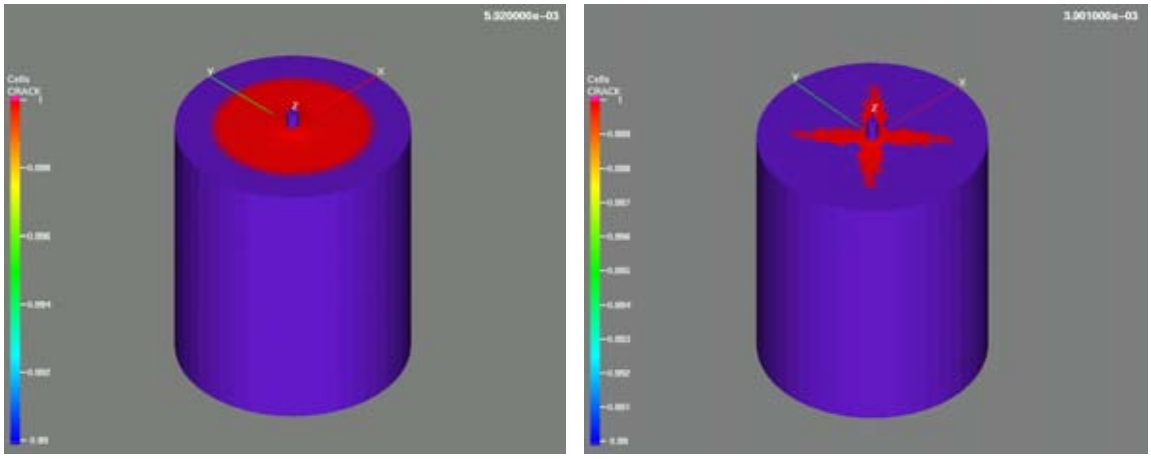

Figure 4-17 The figure on the left shows a contour plot of the cracked region emanating away from the penetrator when the joints are turned off. For comparison, the figure on the right shows the same contour plot when three orthogonal sets of joints are included (baseline case).

4.5.10 Tensile Cracking Turned Off

Figure 4-19 shows that turning the tensile cracking option off caused a surprising increase in predicted penetration depth, albeit quite small, i.e., less that 2 %. The explanation for this is that tensile cracking causes more dilatation of the rock adjacent to the penetrator than the case when there is no tensile cracking thereby inducing higher Coulomb frictional forces on the penetrator. This can clearly be seen in the contour plots of dilatational volume strain in Figure 4-20. There is more dilatation for the case with tensile cracking (baseline case) than the case with tensile cracking turned off. The region

of higher dilatation, however, is relatively small consistent with the relatively small affect on penetration depth predictions.

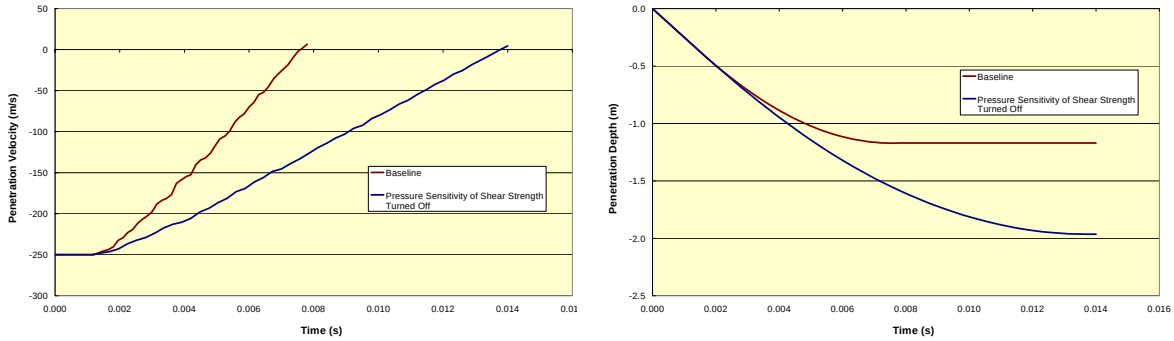

Figure 4-18 The plot on the left shows the velocity of the penetrator versus time while the plot on the right shows the penetration depth versus time. The baseline predictions are shown for comparison with the predictions made with the pressure dependence of shear strength turned off.

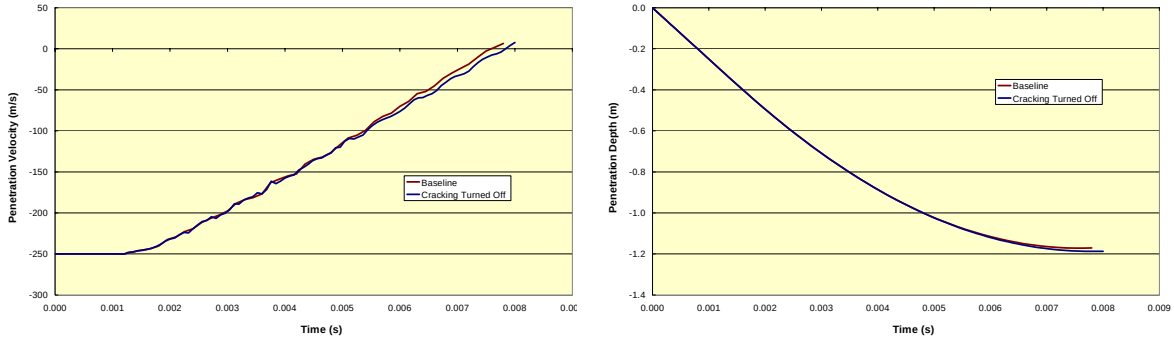

Figure 4-19 The plot on the left shows the velocity of the penetrator versus time while the plot on the right shows the penetration depth versus time. The baseline predictions are shown for comparison with the predections made with the tensile cracking turned off.

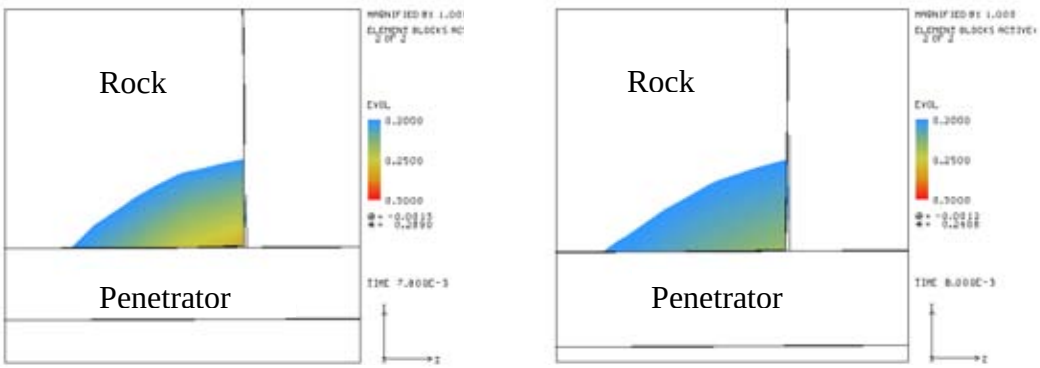

Tensile Cracking Included Tensile Cracking Not Included

Figure 4-20 Tensile cracking results in more dilatational volume strain resulting in less penetration depth prediction because of increased frictional forces. This effect is relatively minor.

4.5.11 Penetrator/Rock Coefficient of Friction Turned Off

Figure 4-21 shows that there is about a 50% increase in predicted penetration depth when the coefficient of friction between the penetrator and the rock is zet to zero. While this friction coefficient is not a material parameter of the rock model per se, it is nonetheless an important contributor in penetration depth calculations and must be estimated in some manner.

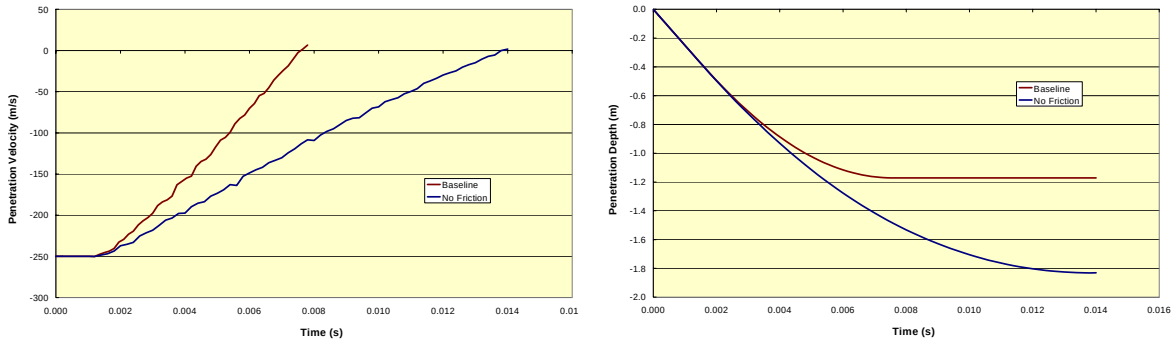

Figure 4-21 The plot on the left shows the velocity of the penetrator versus time while the plot on the right shows the penetration depth versus time. The baseline predictions are shown for comparison with the predections made with the friction between the rock and the penetrator turned off. There is nearly a 50% increase in predicted penetration depth.

4.3 Penetration Depth Versus Striking Velocity

Projectile penetration depth depends strongly on striking velocity. The analyses to this point have been carried out using a striking velocity of 250 m/s. Figure 4-22 illustrates the penetration depth dependence on striking velocity. In general, the penetration depth increases nonlinearly with increasing striking velocity. This figure also shows that if the striking velocity is too low, the penetrator will ricochet off the target.

4.4 Summary

Figure 4-23 shows the relative impact that the various physics features of the rock model have on penetration depth predictions. By far the most important physics feature of the penetration predictions is the pressure sensitivity of shear yield strength followed by the friction coefficient between the penetrator and the rock, and ubiquitous rock jointing. Strain-rate sensitivity and pore collapse are also important but not nearly so much as pressure sensitivity of shear yield and friction. However, the importance of pore collapse increases with increasing penetrator striking velocity. Tensile cracking, kinematic hardening, Lode Angle dependence of yield, and nonlinear elasticity have an insignificant impact on penetration depth predictions.

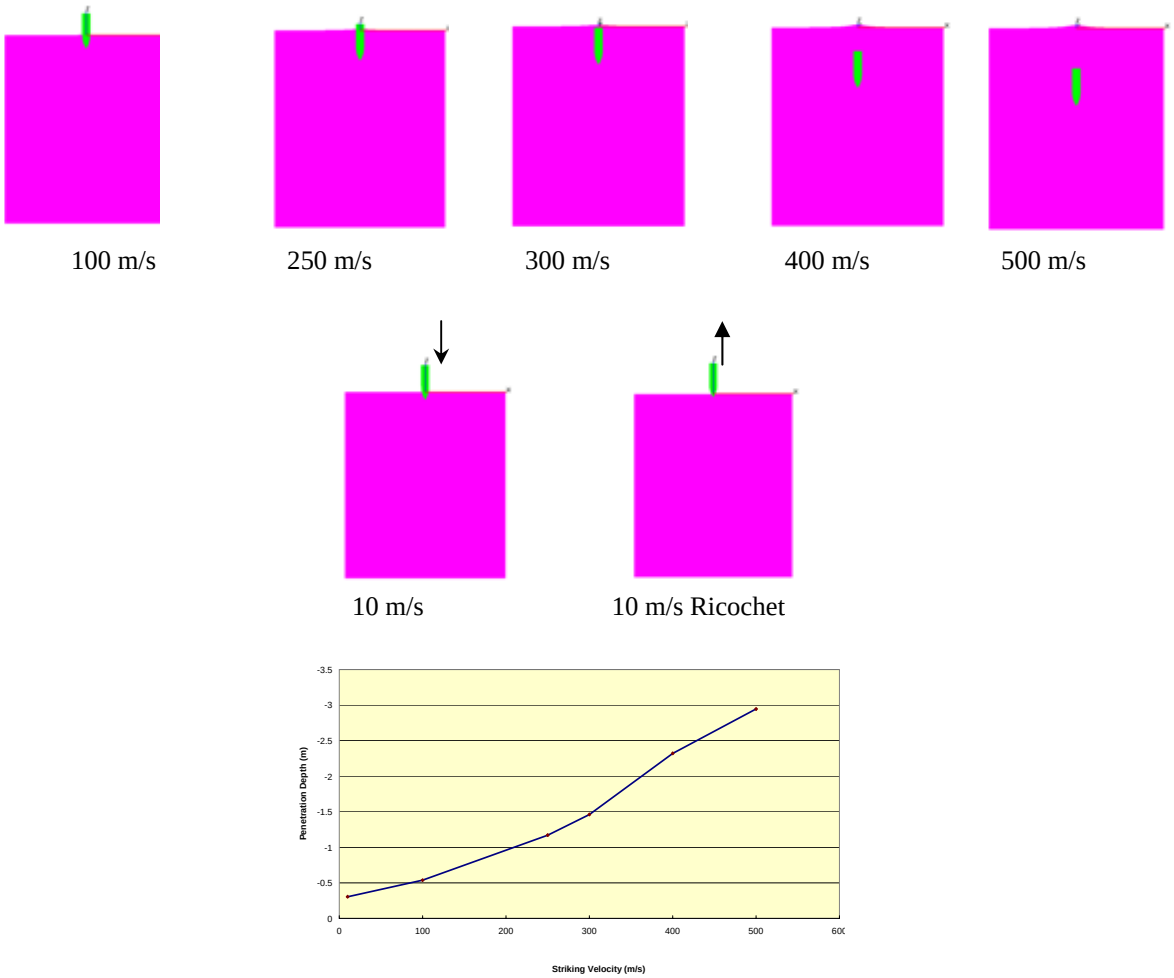

Figure 4-22 Shown is penetration depth versus striking velocity. The projectile bounces off of the target for a striking velocity of 10 m/s.

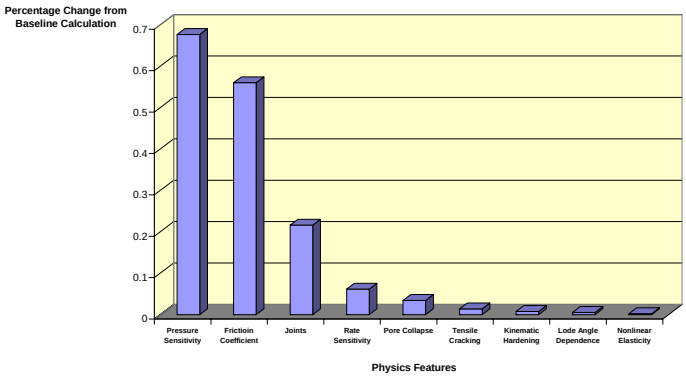

Figure 4-23 This figure shows the relative impact that the physics features of the rock model have on penetration depth predictions. The magnitude represents the percentage change from the baseline calculation when the feature is turned off.

4.5 Probabilistic Analyses

With the influence of the controlling physics features of the rock model for penetration predictions known from the analyses of the previous section, the uncertainty of the penetration response is now determined based on the uncertainties associated with these dominate physical processes. Based on the work of *Fossum et al, (1995)*, marginal probability density functions and coefficients of variation are assigned to the input random variables. For those parameters that are not included in the earlier work, and without information to the contrary, normal probability density functions are assumed and coefficients of variation are determined from a Delphi approach involving expert opinion. Table 4-2 lists these random input variables with their marginal probability density functions and statistics. In all, there are 11 random variables. For this study, these random variables are assumed to be independent even though some of them may be highly correlated.

Table 4-2. Parameter Distributions and Statistics

Parameter	Probability Density Function	Mean Value	Standard Deviation
B0 (Pa)	Weibull	1.300E+10	1.079E+09
G0 (Pa)	Lognormal	9.865E+09	7.694E+08
A2 (1/Pa)	Lognormal	2.731E-10	5.189E-11
P0 (Pa)	Lognormal	-3.144E+08	-1.729E+07
P3	Lognormal	8.400E-02	4.956E-02
T1 (s)	Normal	4.000E-04	3.200E-05
T2 (1/s)	Normal	8.350E-01	6.680E-02
T6 (s)	Normal	3.000E+00	2.400E-01
CN1 (Pa/m)	Normal	5.000E+09	5.000E+08
SP1 (m)	Normal	5.000E-02	2.000E-02
COEF	Normal	4.000E-02	1.600E-02

Probabilistic approaches provide information on whether or not the predicted response, penetration depth in this case, has sufficient confidence and which random variables are most important to control, if possible, from the standpoint of reducing uncertainty. One useful probabilistic measure is the marginal cumulative distribution function (CDF) for the response. The CDF, by definition, quantifies the probability that a chosen response is less than or equal to some specified value. Here, we apply advanced reliability techniques (e.g., *Fossum and Munson, 1996*; *Fossum et al., 1991*) to assess the effect of uncertainties in key rock parameters. To provide a more realistic probabilistic analysis, the number of random variables could be increased to include more material parameters and density, boundary conditions, and loading (such as penetrator striking velocity).

4.4.3 Deterministic Sensitivities

To perform a probabilistic analysis, it is necessary to have a deterministic limit-state (performance) function, which can be defined explicitly when an exact solution is known, or implicitly when an exact solution is not known. In the implicit case such as the one presented here, a numerical solution is used to determine the sensitivity of the structural

response to perturbations of the random variables. This information is then used to construct an empirical explicit function that is used in the advanced reliability approach.

To present the results of the sensitivity analysis, the sensitivities are non-dimensionalized as $(\Delta R/\Delta P)/(P/R)$, where $\Delta R/\Delta P$ represents the change in the response with respect to a change in a specific parameter where R is the response and P the specific parameter. Figure 4.23 shows these relative response sensitivities. Thus in a deterministic sense, the most influential parameters are the parameters associated with rate sensitivity. The next most important parameters are those that represent the ubiquitous joints followed by the coefficient of friction between the penetrator and the rock. The relative importance of the key parameters may be different for a probabilistic analysis depending on the probability density function and the statistics of the parameters.

4.4.4 Probabilistic Results

As described by *Fossum and Munson, 1996* the advanced reliability method that is used here requires (n + 1 + m) finite element calculations, where n equals the number of random variables (11 are considered here), and m equals the number of CDF values selected to cover sufficient probability range (chosen to be 11 in the current work). Thus, the probabilistic analysis required 23 finite element calculations.

The CDF calculated for the penetration depth is shown in Figure 4-25. Figure 4-26 shows the relative probabilistic importance factors for each of the 11 random variables. The CDF shows that there is a probability of 1% that the depth of penetration is greater than or equal to 1.36 meters, and a 99% probability that it is greater than or equal to 1.08 meters. The 50% probability level gives a penetration depth of 1.179, which is only slightly different from the baseline value, which made use of the mean values of the parameters. The reason for the slight difference is that some of the random variables had non-Gaussian probability density functions. Had all of the random variables been normally distributed, the mean value prediction would have agreed with the median (50% probability) prediction.

The uncertainty in the input random variables translates into uncertainty in the predicted response; i.e., depth of penetration. In light of the uncertainty analysis, there is a 98% probability that the depth of penetration lies between –1.36 and –1.08, for a striking velocity of 250 m/s, a difference of 27%. It should be expected that for rocks with more variability (those with higher coefficients of variation) the uncertainty in the response would be greater.

The probabilistic importance factors shown in Figure 4.24 are ordered differently from the deterministic relative response sensitivities, shown in Figure 4.22, and illustrate the importance of uncertainty in the assessment of key parameters. Were it not for the uncertainties in the parameters, the strain-rate sensitive parameters would be the most important parameters controlling penetration depth predictions, but because of uncertainties the joint spacing is the most influential parameter.

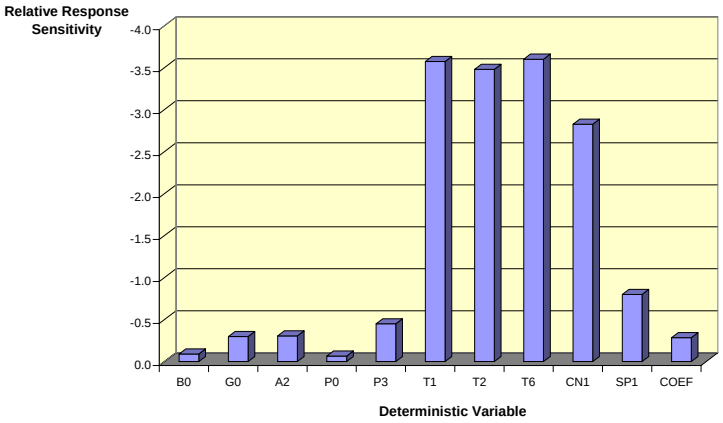

Figure 4-24 Deterministic relative response sensitivities

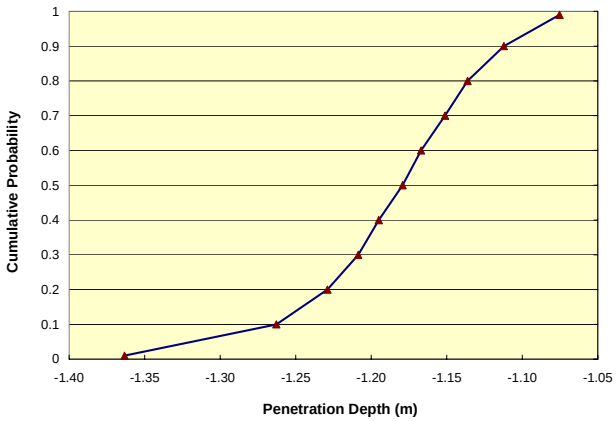

Figure 4-25 This is a plot of the Cumulative Distribution Function (CDF) for penetration depth.

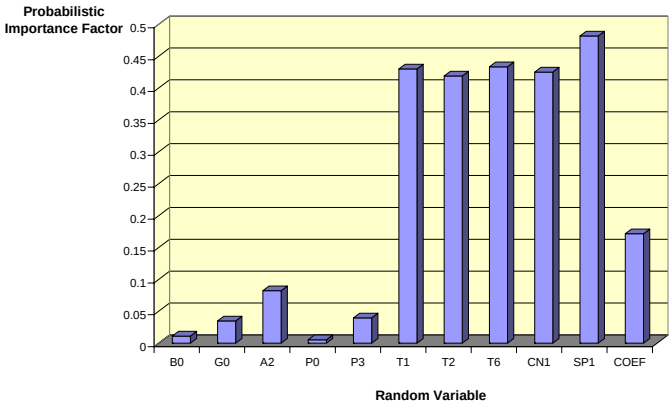

Figure 4-26 Probabilistic importance factors

5. Summary and Conclusions

A realistic, general-purpose rock model that captures the relevant physics observed in standard laboratory quasi-static and dynamic experiments, was developed for use in projectile penetration depth predictions. The rock model was fitted to data obtained from experiments conducted on Salem Limestone. Simulations were made of a projectile striking a Salem Limestone target to determine the relative importance on penetration of model physics features representing the deformation mechanisms involved in pore collapse and micro-crack generation. Probability density functions and statistics were assigned to the important parameters representing the key physical processes affecting penetration and a probabilistic analysis was made to quantify the uncertainty in the penetration depth predictions and to determine which of the uncertain input parameters were important from the standpoint of trying to reduce the uncertainty in the predicted response, perhaps through additional testing.

It was found that the most important physics features of the rock model were pressure sensitivity of shear yield strength followed by the coefficient of friction between the penetrator and the rock[1], ubiquitous rock jointing, strain-rate sensitivity, and pore collapse. From a deterministic standpoint the most important parameters, of those representing the important physics, are those associated with strain-rate sensitivity, while from a probabilistic standpoint, the most important parameters, controlling the uncertainty of the response, are those associated with ubiquitous rock jointing.

The resulting simulation capability resulting from this effort should impact significantly the tools that are needed to design enhanced penetrator systems, support weapons effects studies, and directly address proposed HDBT defeat scenarios. Moreover, the results presented in this report clearly demonstrate the feasibility of analyzing probabilistically the effects that uncertainty in model input parameters have on penetration depth predictions. The advanced reliability methods used in the present study required only 23 finite-element limit-state function evaluations rather than the many thousands that would be required in a sampling-based approach such as a Monte Carlo or an importance sampling approach.

6. Acknowledgments

The technical discussions and programmatic efforts of Dr. Larry Costin on penetration technology are gratefully acknowledged, as are the experimental efforts of Dr. David Holcomb for triaxial extension tests on Salem Limestone, and Dr. Danny Frew for triaxial compression tests and Kolsky Bar dynamic tests on Salem Limestone. The author also acknowledges the important material model discussions with, and the yield surface illustrations of, Dr. Rebecca Brannon. The financial support from Sandia National Laboratories for a Laboratory Directed Research and Development project on penetration is gratefully acknowledged.

[1] The coefficient of friction between the penetrator and the rock is not a material parameter in the rock model that was developed for penetration, but is an important parameter in the structural analysis procedure.

7. References

Fossum, A.F., and R.M. Brannon, "The Sandia GeoModel: Theory and User's Guide," SAND2004-3226, 150 pp, Sandia National Laboratories, Albuquerque, New Mexico, September 2004a.

Fossum, A.F., and R.M. Brannon, "Unified Compaction/Dilatation, Strain-Rate Sensitive Constitutive Model for Rock Mechanics Structural Analysis Applications," *ARMA/NARMS 04-546, 6th North American Rock Mechanics Symposium*, Houston, Texas, 12 pp., June 5-9, 2004b.

Warren, T.L., A.F. Fossum, and D.J. Frew, "Penetration into Low-Strength (23 MPa) Concrete: Target Characterization and Simulations," *Int. J. of Impact Engr., 30*, pp. 477-503, 2004.

Fossum, A.F., P.E. Senseny, T.W. Pfeifle, K.D. Mellegard, "Experimental Determination of Probability Distributions for Parameters of a Salem Limestone Cap Plasticity Model," *Mech. of Mat. 21*, pp. 119-137, 1995.

Frew, D.J., M.J. Forrestal, and W. Chen, "A Split Hopkinson Pressure Bar Technique to Determine Compressive Stress-Strain Data for Rock Materials," *Exp. Mech., 41,* pp. 40-60, 2001.

Fossum, A.F., and D.E. Munson, "Probabilistic Creep Analysis of Underground Structures in Salt," *J. of Engr. Mech., 122,* pp. 209-217.

Fossum, A.F., P.E. Senseny, and B.H. Thacker, "Input Uncertainties and Calculated Borehole Closure," *Proc., 29th Symp. on Rock Mech.,* Norman, Okla., pp. 987-994, 1991.

DISTRIBUTION:

External

Internal
MS9018 Central Technical File, 8945-1
MS0899 Technical Library, 9616 (2)
MS0751 A.F. Fossum, 6117 (5)
MS0751 L.S. Costin, 6117 (5)
MS0751 R.M. Brannon, 6117
MS0751 K. Gaither, 6117
MS0751 D.J. Holcomb, 6117
MS0417 A.R. Lappin, 6117
MS0751 M.Y. Lee, 6117
MS0751 W.A. Olsson, 6117
MS0751 T.W. Pfeifle, 6117
MS0751 S.R. Sobolik, 6117
MS0751 O.E. Strack, 6117
MS0706 D.J. Borns, 6113
MS0735 R.E. Finely, 6115
MS0750 G.J. Elbring, 6116
MS1160 D.A. Dederman, 15412
MS1160 D.J. Frew, 15412
MS1160 M.J. Forrestal, 15412
MS1160 T.L. Warren, 15412
MS1174 J.T. Hitchcock, 15403
MS1164 D.L. Keese, 15404
MS0376 J.G. Arguello, 9126
MS0376 C.M. Stone, 9127
MS0372 J. Jung, 9127
MS0372 D.B. Longcope, 9127
MS0893 J. Pott, 9123
MS0378 R.M. Summers, 9231
MS0378 S.P. Burns, 9231
MS0316 P. Yarrington, 9230
MS9042 M.L. Chiesa, 8774